ASME Journal of Dynamic Systems, Measurement, and Control
Online journal at:
https://asmedigitalcollection.asme.org/dynamicsystems

Control Oriented Modeling, Experimentation, and Stability Analysis of an Autorotating Samara

Jonathan McConnell
Mechanical Engineering,
University of Central Florida,
4000 Central Florida Building,
Orlando, FL 32816
e-mail: jonathan.mcconnell@knights.ucf.edu

Tuhin Das
Associate Professor
Mechanical and Aerospace Engineering Department,
University of Central Florida,
Orlando, FL 32816
e-mail: tuhin.das@ucf.edu

This paper presents a control-oriented model for describing the steady-state and dynamic behavior of a single-winged samara seed-pod in autorotative descent. A negligible lateral center of mass motion and constant, prescribed roll-angle to develop a simplified and compact model. Spanwise aerodynamic dependence is exchanged for an independent blade element representation with two tuned parameters to account for the effects of leading-edge vortex phenomena. The resulting model is a fourth-order nonlinear dynamical system. The accuracy of this model is established by validating it against our own experimental data as well as against those reported in the literature by other researchers. The validation exercise reveals that zero roll-angle is a viable assumption that significantly reduces model complexity while retaining accuracy. A necessary condition is derived for the existence of steady autorotation of the samara under free descent. Furthermore, a stability analysis is conducted suggesting that the eigenvalues of the fourth-order system, linearized about the autorotational equilibrium, can be well-represented by those of two decoupled two-dimensional systems. The analysis reveals the critical parameters that determine stability of sustained autorotation. Such stability analysis provides a platform for similar analytical exploration of future model improvements. The validity of this compact model suggests the plausibility of designing and controlling simple autorotative mechanisms based on these dynamics. [DOI: 10.1115/1.4062438]

1 Introduction

Samara seed pods, a morphology that has evolved parallel in numerous plants throughout the world, effectively employ autorotation to slow descent speed. This allows organisms to produce heavier seeds/fruit that can be scattered across a larger area by prevailing winds and gusts, [1–6]. The study of these biological structures can provide insight into efficient design of aerodynamic systems, both small and large. Samaras can be classified by wing configuration and aerodynamic behavior in descent [7]. This paper will focus on samars of the single-winged variety that do not roll about their spanwise axis at steady-state.

A seminal work by Norberg [8], has presented a thorough qualitative and experimental analysis of samara stability. However, through dynamic modeling, a mathematical analysis can be performed to draw more quantitative insight in regards to samara descent behavior, e.g., ranges of physical and aerodynamic parameters that allow for stable autorotation. A simple mathematical analysis of samara stability was presented in Ref. [9] for the purpose of modeling and controlling a powered single-winged rotorcraft. This work was further expanded upon in Ref. [10]. Computational fluid dynamics was utilized in Refs. [11] and [12] to analyze the microscale effects of turbulence and leading-edge vortices. Discussion of the effects of leading-edge vortices and the robustness of samara stability to gusts has been given in Ref. [13]. An extensive and detailed model of samara dynamics and an analysis of stability have been presented by Rosen and Seter [14,15], which employ blade element method with special attention to the effects of low Reynolds number. Further experimental work can be found in Refs. [4], [12], [14], [16], and [17].

It is the goal of this paper to provide a more compact blade element theory-based model for a samara in vertical descent by neglecting lateral movement and assuming negligible roll angle. This model, presented in Sec. 2, is explored for analysis of both steady-state, and transient behavior. Expanding upon the work in Ref. [18], an experimental setup and results are discussed in Sec. 3 for tuning and validation of simulation results. Furthermore, an analytical derivation of conservative boundaries for aerodynamic and physical properties that allow steady autorotation is discussed in Sec. 4, and a stability analysis of the autorotational equilibrium is conducted in Sec. 5. This is followed by Concluding Remarks, Acknowledgments, References, and an Appendix, in that order. The paper provides a model that balances accuracy and ease of implementation for stability analysis as well as design and control of simple single-winged rotorcraft similar to that of Refs. [9], [10], [19], and [20].

2 Modeling

2.1 Dynamic Model. The equations of motion with respect to a body-fixed reference frame are displayed in the following equations:

Contributed by the Dynamic Systems Division of ASME for publication in the Journal of Dynamic Systems, Measurement, and Control. Manuscript received September 2, 2022; final manuscript received April 14, 2023; published online May 15, 2023. Assoc. Editor: Amit K. Sanyal.

$$
\begin{aligned}
I_{x_3x_3}\,\dot{\omega}_{x_3} + (I_{z_3z_3} - I_{y_3y_3})\omega_{y_3}\,\omega_{z_3} &= M_{x_3}\\
I_{y_3y_3}\,\dot{\omega}_{y_3} + (I_{x_3x_3} - I_{z_3z_3})\omega_{x_3}\,\omega_{z_3} &= M_{y_3}\\
I_{z_3z_3}\,\dot{\omega}_{z_3} + (I_{y_3y_3} - I_{x_3x_3})\omega_{x_3}\,\omega_{y_3} &= M_{z_3}
\end{aligned}
\tag{1}
$$

$$
\begin{aligned}
m\dot{v}_0 = &-mg + F_{x_3}\,\sin\,\theta\\
&+ F_{y_3}\,\sin\,\psi\,\cos\,\theta + F_{z_3}\,\cos\,\psi\,\cos\,\theta
\end{aligned}
\tag{2}
$$

where $I_{x_3x_3}$, ω_{x_3}, and M_{x_3} refer to the moment of inertia, angular velocity, and net moment about the body-fixed x-axis, and F_{x_3} refers to the net force in the direction of the body-fixed x-axis. The same naming convention follows for the body-fixed y- and z-axes. The angular velocity of the samara in the body-fixed frame (x_3, y_3, z_3) can be expressed using Euler angles as follows:

$$
\begin{aligned}
\boldsymbol{\omega} &= \omega_{x_3}\hat{i} + \omega_{y_3}\hat{j} + \omega_{z_3}\hat{k}\\
&= (\dot{\psi} + \dot{\phi}\sin\theta)\hat{i} + (\dot{\phi}\cos\theta\sin\psi - \dot{\theta}\cos\psi)\hat{j}\\
&\quad + (\dot{\phi}\cos\theta\cos\psi + \dot{\theta}\sin\psi)\hat{k}
\end{aligned}
\tag{3}
$$

The forces F_{x_3}, F_{y_3}, F_{z_3} and the moments M_{x_3}, M_{y_3}, M_{z_3} are due to aerodynamics. To determine them, the position and velocity of a point P shown in Fig. 1(*a*) can be expressed relative to O as given below:

$$
\begin{aligned}
&\mathbf{r_P} = \mathbf{r_O} + r\hat{i}, \quad \mathbf{v_P} = \mathbf{v_O} + (\boldsymbol{\omega} \times r\hat{i})\\
&\mathbf{v_O} = v_o(\sin\theta\hat{i} + \cos\theta\cos\psi\hat{j} + \cos\theta\sin\psi\hat{k})
\end{aligned}
\tag{4}
$$

In Eq. (4) it is assumed that the point O of the samara has motion predominantly in the vertical direction with negligible motion in lateral directions. From Eqs. (3) and (4)

$$
\begin{aligned}
\mathbf{v_P} &= \mathbf{v_O} + (\boldsymbol{\omega} \times r\hat{i})\\
&= v_o\sin\theta\hat{i} + [v_o\cos\theta\cos\psi - r(\dot{\phi}\cos\theta\sin\psi - \dot{\theta}\cos\psi)]\hat{k}\\
&\quad + [v_o\cos\theta\sin\psi + r(\dot{\phi}\cos\theta\cos\psi + \dot{\theta}\sin\psi)]\hat{j}
\end{aligned}
\tag{5}
$$

The wind velocity relative to P is assumed $\mathbf{v_{W/P}} = -\mathbf{v_P}$. This approximation neglects the effects of the leading edge vortex of a single-winged samara which couples blade elements. Efforts were made in Ref. [14] to account for spanwise flow with skewed blade elements. Instead, a corrective tuning adjusts the coefficient of drag and moment of inertia for the effects of the coupled aerodynamics. This correction will be discussed further in Secs. 2.2 and 3.2. From Fig. 2 for an element along the samara blade, the local drag and lift forces, dD and dL, respectively, are given by

$$
\begin{aligned}
dD &= \frac{1}{2}\rho w(r)drC_D(\alpha)||\mathbf{U}_\infty||^2\\
dL &= \frac{1}{2}\rho w(r)drC_L(\alpha)||\mathbf{U}_\infty||^2
\end{aligned}
\tag{6}
$$

where α is the spanwise local angle of attack and from Eq. (5)

$$
\mathbf{U}_\infty = -v_{P,y}\hat{j} - v_{P,z}\hat{k} \quad \text{and} \quad \tan\alpha = -\frac{v_{P,z}}{v_{P,y}}
\tag{7}
$$

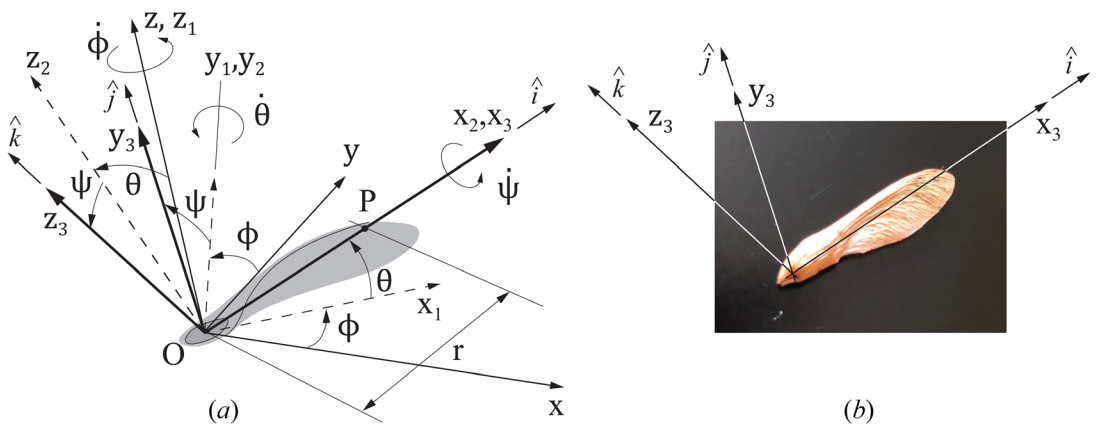

Fig. 1 Euler angle definition for a samara

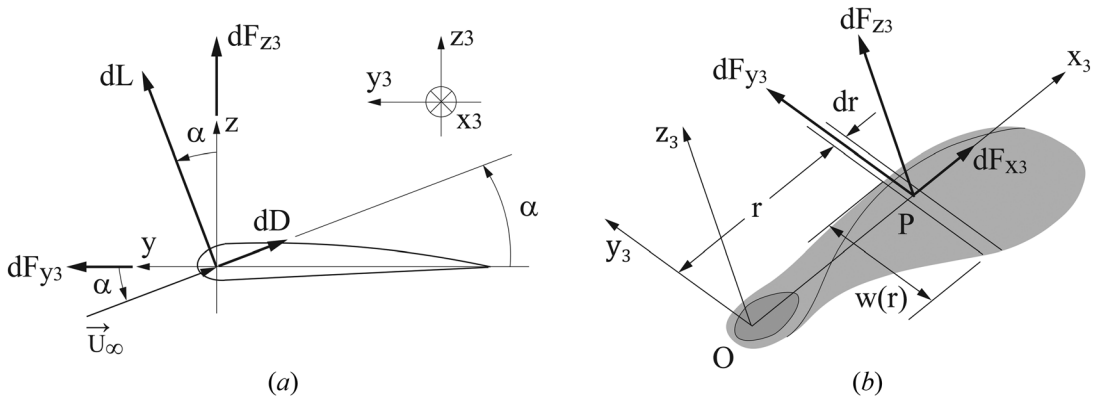

Fig. 2 Elemental forces on a blade

where $\mathbf{U}_\infty$ is the relative wind velocity experienced by a blade element (see Fig. 2). The element forces in body-fixed y_3 and z_3 directions are

$$\begin{aligned} dF_{y_3} &= \frac{1}{2}\rho w(r)||\mathbf{U}_\infty||^2(\sin\alpha\, C_L(\alpha) - \cos\alpha\, C_D(\alpha))dr \\ dF_{z_3} &= \frac{1}{2}\rho w(r)||\mathbf{U}_\infty||^2(\cos\alpha\, C_L(\alpha) + \sin\alpha\, C_D(\alpha))dr \end{aligned} \tag{8}$$

The overall forces and moments are

$$\begin{aligned} F_{y_3} &= \int_{r_0}^{r_f} dF_{y_3}, \qquad F_{z_3} = \int_{r_0}^{r_f} dF_{z_3} \\ M_{z_3} &= \int_{r_0}^{r_f} r\, dF_{y_3}, \quad M_{y_3} = -\int_{r_0}^{r_f} r\, dF_{z_3} \end{aligned} \tag{9}$$

2.2 Simplifying Assumptions. In Eq. (9), note that the limits of integration r_0 and r_f are not equal to 0 and R, respectively. This is because, as evident from Fig. 1(*b*), the wing-span that contributes to the aerodynamic forces starts from $r_0 > 0$ and ends at an $r_f < R$. The bottom boundary of r_0 is taken to account for losses due to the rounded seed geometry near the center of mass, whereas the top boundary of r_f is taken to account for tip losses. For practicality, constant values have been selected for r_0 and r_f as ratios of a given samara's radius, R (see Table 3). Also, as the forces and moments are resolved, the following two simplifying assumptions are applied:

(1) The effect of dF_{x_3}, the elemental force along the blade span, is neglected. Thus, $F_{x_3} \approx 0$ is assumed and its effect on aerodynamics is neglected. This simplifies the dynamic model. The assumption can be removed by using the net relative wind velocity on the (x_3, y_3) plane and accordingly considering blade elements to be tilted from the y_3 axis instead of being parallel to it, as shown in Fig. 2(*b*).
(2) The rolling moment is assumed $M_{x_3} \approx 0$. This is based on the observation that the samara's motion is dominated by the yaw rate $\dot{\phi}$, the pitching motion $\theta, \dot{\theta}$ (coning), and the vertical motion v_0.

A samara is typically an elongated and planar rigid body. Thus, for simplicity $I_{z_3z_3} = I_{x_3x_3} + I_{y_3y_3}$ can be applied. Moreover, due to the slender thickness and planform of the samara blade, it is assumed that the moment of inertia with respect to the spanwise axis, $I_{x_3x_3} \ll I_{y_3y_3}, I_{z_3z_3}$. Accordingly, this work assumes $I_{x_3x_3} = 0$ and $I_{z_3z_3} = I_{y_3y_3}$. It is important to note that the mass of the samara is not evenly distributed. A majority of its mass is concentrated at the seed, at point O (see Figs. 1(*a*) and 1(*b*)). It is imperative that this be taken into consideration when approximating the value for $I_{y_3y_3}$. For this paper, Eq. (10) was employed for moment of inertia approximation

$$I_{y_3y_3} = \frac{1}{3}fmR^2 \tag{10}$$

where f is a tunable factor to account for the nonuniform mass distribution which differs from samara to samara. The resulting reduced moment of inertia helps achieve coning angles that correlate well with data published in the literature, [8]. For the purposes of producing a simplified model, the center of mass is taken to be at O.

As mentioned in Sec. 2.1, the integration of independent blade elements perpendicular to the span ignores the spanwise airflow of the leading edge vortex which has been documented for single-winged samara structures [11–13]. This simplification is emphasized by assumption 1 (above) which states that $F_{x_3} \approx 0$. It will be shown in Sec. 3 that a strong agreement with steady-state values can be achieved with corrective adjustment of two tunable parameters: f from Eq. (10) and later C_{D_0} from Eq. (19). The goal of this model is to provide a platform for reaching accurate steady-state results with realistic dynamic behavior. It is expected that a direct implementation of leading-edge vortex aerodynamics would improve the predictive accuracy of the model for the extreme dynamics before settling into autorotation. This addition would, however, significantly increase model complexity which can be detrimental to control applications.

Through observation of a samara in descent, it is seen that the roll angle, ψ, remains small. With this observation, and consideration of the symmetry of the samara's airfoil profile, it is reasonable to assume that the angle ψ will be nearly if not exactly zero at steady-state. Further, the assumption of $M_{x_3} \approx 0$ along with $I_{x_3x_3} = 0$ and $I_{z_3z_3} = I_{y_3y_3}$ implies that the first equation of Eq. (1) is identically zero. The dynamics and statics of the system can be studied for different constant values of ψ. Statics analysis reveals that only a small range of ψ around zero is allowable. This simplification reduces the statics problem to that of determining three unknowns, namely, $\dot{\phi}$, θ, and v_0. The dynamics reduce to four states, namely, $\dot{\phi}$, $\dot{\theta}$, θ, and v_0. The simplified dynamics of an autorotating samara are next provided. From the second and third equations of Eq. (1), from Eq. (2), and imposing $\dot{\psi} = 0$ on ω_{x_3}, ω_{y_3}, ω_{z_3} in Eq. (3)

$$\begin{aligned} &\ddot{\theta}\cos\psi + \dot{\phi}^2\sin\theta\cos\theta\cos\psi + 2\dot{\phi}\dot{\theta}\sin\theta\sin\psi \\ &\quad - \ddot{\phi}\cos\theta\sin\psi = -M_{y_3}/I_{y_3y_3} \\ &\ddot{\theta}\sin\psi + \dot{\phi}^2\sin\theta\cos\theta\sin\psi - 2\dot{\phi}\dot{\theta}\sin\theta\cos\psi \\ &\quad + \ddot{\phi}\cos\theta\cos\psi = M_{z_3}/I_{y_3y_3} \\ &\dot{v}_0 = -g + (F_{y_3}\cos\theta\sin\psi)/m + (F_{z_3}\cos\theta\cos\psi)/m \end{aligned} \tag{11}$$

where M_{y_3}, M_{z_3} and F_{z_3} are nonlinear functions of the state variables, as given in Eqs. (8) and (9). It is noted here from Eqs. (5), (6), and (7) that

$$\begin{aligned} ||U_\infty||^2 &= r^2\dot{\phi}^2\cos^2\theta + (r\dot{\theta} + v_0\cos\theta)^2 \\ \sin\alpha &= [-v_0\cos\theta\cos\psi + r(\dot{\phi}\cos\theta\sin\psi - \dot{\theta}\cos\psi)]/||U_\infty|| \\ \cos\alpha &= [v_0\cos\theta\sin\psi + r(\dot{\phi}\cos\theta\cos\psi + \dot{\theta}\sin\psi)]/||U_\infty|| \end{aligned} \tag{12}$$

2.3 Conditions For Steady Autorotation. Conditions for steady autorotation can now be derived from the dynamic model above by imposing $\ddot{\theta} = \ddot{\phi} = \dot{\theta} = \dot{v}_0 = 0$. It is noted here, that in deriving the conditions for steady autorotation, the roll angle, ψ, is allowed to assume nonzero constant values. The value, ψ, is treated as an input in determining the possible set of autorotational equilibria. The exercise confirms that feasible steady values of ψ lie only a few degrees around $\psi = 0$. The equations for steady autorotation, obtained from Eqs. (1)–(3) are

$$\begin{aligned} \dot{\phi}^2\sin\theta\cos\theta\cos\psi &= -M_{y_3}/I_{y_3y_3} \\ \dot{\phi}^2\sin\theta\cos\theta\sin\psi &= M_{z_3}/I_{y_3y_3} \\ mg &= F_{y_3}\sin\psi\cos\theta + F_{z_3}\cos\psi\cos\theta \end{aligned} \tag{13}$$

The static model in Eq. (13) can be expressed in a compact form by the introduction of two dimensionless parameters, given in the following equation:

$$\chi = \frac{r}{R}, \quad \lambda = -\frac{v_0}{\dot{\phi}R} \tag{14}$$

The ratio χ represents the span-ratio which is the position of a blade element with respect to the length of the blade. The ratio λ represents the tip-speed-ratio which is the relation of the vertical descent speed to the speed of the tip of the blade. The ratio λ/χ produces a local speed ratio which describes the relation of the vertical descent speed of the entire samara to the local velocity of a blade element. Inclusion of the local speed ratio provides insight into spanwise characteristics. Applying the ratios in Eq. (14) produce the following expressions for the local $||U_\infty||$ and α under steady autorotation:

$$
\begin{aligned}
||U_\infty||^2 &= r^2\dot{\phi}^2\cos^2\theta\left[1+\left(\frac{\lambda}{\chi}\right)^2\right] \\
\sin\alpha &= \left(r\dot{\phi}\sin\psi - v_0\cos\psi\right)\cos\theta/||U_\infty|| \\
\cos\alpha &= \left(r\dot{\phi}\cos\psi + v_0\sin\psi\right)\cos\theta/||U_\infty|| \\
\Rightarrow \tan\alpha &= \left(\tan\psi + \frac{\lambda}{\chi}\right)\Big/\left(1-\tan\psi\frac{\lambda}{\chi}\right)
\end{aligned}
\tag{15}
$$

It should be noted here that for negligible ψ, the right-hand side of Eq. (15) reduces to the local speed ratio of the blade element. Expanding Eq. (13) using Eqs. (8), (9), and (15) produces the following system of equations:

$$
\begin{aligned}
M_{y_3} &= -I_{y_3y_3}\dot{\phi}^2\sin\theta\cos\theta\cos\psi \\
&= -\frac{1}{2}\rho\dot{\phi}\cos^2\theta\int_{r_0}^{r_f} r^3 w(r)\sqrt{1+\left(\frac{\lambda}{\chi}\right)^2} \\
&\quad\left[\left(\frac{\lambda}{\chi}C_L(\alpha)+C_D(\alpha)\right)\sin\psi\right. \\
&\quad\left.-\left(C_L(\alpha)-\frac{\lambda}{\chi}C_D(\alpha)\right)\cos\psi\right]dr
\end{aligned}
\tag{16}
$$

$$
\begin{aligned}
M_{z_3} &= I_{y_3y_3}\dot{\phi}^2\sin\theta\cos\theta\sin\psi \\
&= \frac{1}{2}\rho\dot{\phi}\cos^2\theta\int_{r_0}^{r_f} r^3 w(r)\sqrt{1+\left(\frac{\lambda}{\chi}\right)^2} \\
&\quad\left[\left(C_L(\alpha)+\frac{\lambda}{\chi}C_D(\alpha)\right)\sin\psi\right. \\
&\quad\left.+\left(\frac{\lambda}{\chi}C_L(\alpha)-C_D(\alpha)\right)\cos\psi\right]dr
\end{aligned}
\tag{17}
$$

$$
\begin{aligned}
mg &= \frac{1}{2}\rho\dot{\phi}\cos^2\theta\int_{r_0}^{r_f} r^2 w(r)\sqrt{1+\left(\frac{\lambda}{\chi}\right)^2} \\
&\quad\left[\left(-\frac{\lambda}{\chi}C_L(\alpha)+C_D(\alpha)\right)\sin\psi\right. \\
&\quad\left.+\left(C_L(\alpha)+\frac{\lambda}{\chi}C_D(\alpha)\right)\cos\psi\right]dr
\end{aligned}
\tag{18}
$$

Here a simple thin airfoil model is employed to select values for C_L and C_D, the coefficients of lift and drag, respectively [21]. Specifically

$$
\begin{aligned}
C_L(\alpha) &= 2\pi\sin\alpha \\
C_D(\alpha) &= C_L(\alpha)\sin\alpha + C_{D_0}
\end{aligned}
\tag{19}
$$

where C_{D_0} is a tuned additional drag to account for the effects of roughness and airfoil thickness. Traditionally, Eq. (19) is representative of potential flow with no flow separation. This simplification does not consider the presence of a leading edge vortex, however, it has been seen from comparison to literature that the trends of Eq. (19) are behaviorally comparable to that of low Reynolds Number flow over small wings, [14]. It is shown in Sec. 3.2 that accurate equilibrium values are achieved after system tuning without deviating from realistic values of C_{D_0}. Equations (16)–(18) can be numerically solved for the steady-state values of $\dot{\phi}$, θ, v_0, and λ for a range of values of ψ. The process of determining the steady conditions is to first solve for λ from Eqs. (16) and (17). This is done by noting that

$$
M_{z_3}\cos\psi + M_{y_3}\sin\psi = 0 \tag{20}
$$

Equation (20) must be solved numerically to determine the steady value of λ. Once solved, θ can be determined from either Eqs. (16) or (17). Here, θ can be solved explicitly. Next $\dot{\phi}$ can be determined explicitly from Eq. (18). Finally, knowing λ and $\dot{\phi}$, v_0 can also be explicitly determined from the definition of λ in Eq. (14).

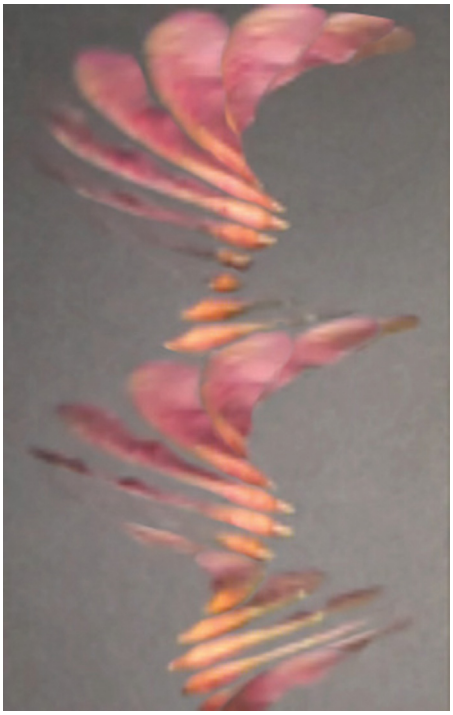

Fig. 3 Visualization of a samara spiral descent

3 Results and Validation

3.1 Experimental Setup and Results. For observation of samara performance and collection of validation data, an experimental setup was created in the following manner:

(1) Samaras were collected from local maple trees (specifically Red Maples—*Acer rubrum*).
(2) A measuring tape was hung plum in camera view of a Samsung Z Fold3.
(3) Samaras were dropped from sufficient height in plane with the measuring tape and recorded at 960 frames per second (visualized in Fig. 3).
(4) Samaras were also recorded from a top-down perspective at the same frame rate.
(5) The collected footage was analyzed frame-by-frame to extract θ, $\dot{\phi}$, and v_0.

It is important to note that for accurate falling speed estimation, samaras should be recorded falling in the same plane as the measuring tape. Analyzing recordings of samaras with significant offset from the distance reference requires correction for parallax effects and can increase error. Furthermore, angle measurements should be taken when the samara is nearest to the center of view, such that minimal perspective distortion is present. A visualization of angle measurement is seen in Fig. 4. A sample video of samara descent from both front and top views is available at the following link.[1]

Performance measurements were conducted for five sample samaras. The physical parameters of this sample group are presented in Table 1, along with the physical parameters of three larger samaras from previous works [8,12]. The parameters f_{opt} and $C_{D_{0_{\text{opt}}}}$ are optimized values and will be discussed in Sec. 3.2. It should be noted that the Norberg and Holden 2 specimens are not Red Maple samaras, but Norway maple (*Acer plantanoides*) and silver maple

[1] https://youtu.be/B9Bl_dBsOIo

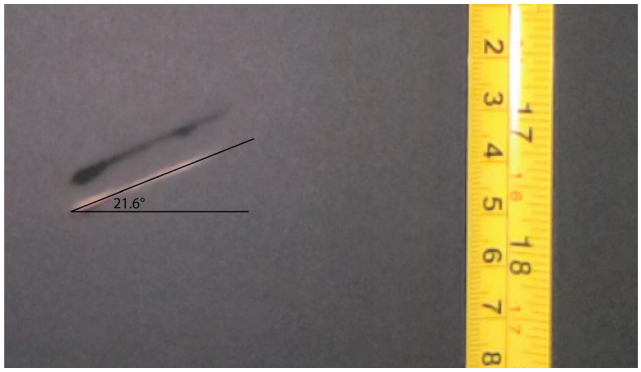

Fig. 4 Visualization of samara pitch angle, θ

Table 1 Samara experimental parameters

	m (kg)	L (m)	R (m)	f_{opt}	$C_{D_0\,\text{opt}}$
Samara 1	0.000031	0.035	0.025	0.209	0.033
Samara 2	0.000025	0.038	0.025	0.359	0.224
Samara 3	0.000022	0.035	0.021	0.402	0.213
Samara 4	0.000046	0.035	0.023	0.326	0.872
Samara 5	0.000038	0.032	0.019	0.329	0.794
Norberg	0.00013	0.047	0.035	0.238	0.124
Holden 1	0.000116	0.040	0.034	0.249	0.219
Holden 2	0.000236	0.059	0.048	0.684	0.708

(*Acer saccharinum*), respectively. Experimental values for steady-state θ, $\dot{\phi}$, and v_0 are presented in Table 2 for the five tested samaras as well as the three samaras from the literature.

3.2 Parameter Optimization. It has been observed that samaras, even within one species, vary significantly in size, mass, curvature, etc. For this reason, selecting an appropriate value for $I_{y_3y_3}$ and C_D is a nontrivial effort. Direct measurement of these values requires microscale testing and in many cases, destruction of a specimen for analysis of mass distribution. For this reason, two tunable parameters have been added, namely, f and C_{D_0} in Eqs. (10) and (19), respectively, to adjust approximations of $I_{y_3y_3}$ and C_D for variation in morphology and higher-order aerodynamic response. Given the model above and collected experimental data, as well as other important modeling parameters listed in Table 3, a two-dimensional steepest descent optimization can be employed to select values for f and C_{D_0}. A successful optimization should not only produce modeled steady-state values of θ, $\dot{\phi}$, and v_0 which show good agreement with experimental values but also produce realistic values for f and C_{D_0}.

Optimized values for the eight studied samaras are presented in Table 1. It can be see in Table 2 that strong agreement is achieved for θ, $\dot{\phi}$, and v_0. For a study of appropriate $I_{y_3y_3}$ values, samara 2 was separated into two pieces: seed and wing. These separate sections were measured for mass and physical dimensions, and an approximation of $I_{y_3y_3}$ was performed by considering the seed to be a cylinder and the wing a rectangular flat plate, each of uniform density. From this analysis, it was found that $I_{y_3y_3} \approx 2 \times 10^{-9}\,\text{kg m}^2$ for samara 2. Due to the rounded geometry of both the seed and wing, the above approximation is an overestimate. Given the measured $I_{y_3y_3}$, Eq. (10) can be used to show $f \approx 0.47$. This value is larger, yet of similar magnitude to the value optimized through steepest descent. The optimized values of C_{D_0} in Table 1 are also realistic, as they are comparable to the low Reynolds Number performance of insect wings [14]. As will be discussed further in Sec. 4, the optimized C_{D_0} values also fall within the necessary range of stability.

Table 3 Samara and environmental parameters

r_0	$0.2R$	m
r_f	$0.9R$	m
ρ	1.225	kg/m^3

3.3 Analysis of Variable Roll. As previously stated, the above steady-state model was produced for an arbitrary roll angle, ψ. This allows for simulation of a range of equilibrium results for a span of ψ values. To explore the effects of varying ψ, the physical parameters of the Norberg specimen (see Table 1) were inputted, and the steady-state values of $\dot{\phi}$, θ, v_0, and λ were modeled for a range of $-15\,\text{deg} < \psi < 15\,\text{deg}$. The results of this analysis are presented in Figs. 5 and 6.

It can be observed in Fig. 5(*a*) that a significant error in steady-state $\dot{\phi}$ is associated with negative ψ. Furthermore, the steep, positive correlation of θ and ψ seen in Fig. 5(*b*) suggests that adjusting ψ by a few degrees to either side of $\psi = 0$ results in a significant deviation of steady-state θ agreement. These trends, however, are produced using the f and C_{D_0} values of Table 1, which were optimized under the assumption of $\psi = 0$. For this reason, an analogous three-dimensional steepest descent algorithm has been employed to not only optimize f and C_{D_0}, but to also allow ψ to vary. For this optimization, the values of Table 1 were taken as initial guesses to see if significant deviation would occur when the assumption of $\psi = 0$ was removed. The results of this process are presented in Table 4. The resulting optimized ψ values do not deviate further than 0.6 deg from 0 deg and produce only minimal improvements in steady-state agreement of θ, $\dot{\phi}$, and v_0. Furthermore, the variability in magnitude and sign of the optimized ψ suggests that such a correction is specific to individual morphological differences among samaras rather than suggesting a innate, nonzero roll for all samaras.

3.4 Dynamics Simulations. The transient behavior of a falling samara is next studied through simulations. Steady-state analysis has shown that it is reasonable to assume $\psi = 0$ near equilibrium. It has been observed that a falling samara establishes autorotation in a matter of a few seconds. This coupled with the minuscule rolling moment of inertia, $I_{x_3x_3}$, suggests that achieving negligible roll angle will be nearly instantaneous. It is therefore reasonable for this control-oriented model to extend the assumption of $\psi = 0$ to transients. For consistency with the steady-state analysis, ψ has been

Table 2 Samara experimental and modeled results: θ (deg), $\dot{\phi}$ (rev/s), and v_0 (m/s)

	θ_{exp}	θ_{mod}	θ_{PE}	$\dot{\phi}_{\text{exp}}$	$\dot{\phi}_{\text{mod}}$	$\dot{\phi}_{\text{PE}}$	$v_{0\,\text{exp}}$	$v_{0\text{mod}}$	$v_{0\text{PE}}$
Samara 1	21.6	21.6	0.08%	16.6	16.4	0.64%	–0.55	–0.50	9.66%
Samara 2	24.6	24.6	0.03%	12.3	12.5	–1.16%	–0.62	–0.61	2.38%
Samara 3	19.0	19.1	–0.10%	12.9	13.4	–3.47%	–0.57	–0.59	–1.91%
Samara 4	29.8	29.7	0.18%	12.1	12.4	–2.79%	–1.16	–0.95	18.42%
Samara 5	19.9	20.0	–0.31%	15.1	15.1	–0.58%	–0.87	–0.92	–5.70%
Norberg	20	20.0	–0.02%	13	13.3	–2.15%	–0.9	–0.82	8.43%
Holden 1	24	24.0	0.14%	12.0	12.5	–3.51%	–0.98	–0.88	10.17%
Holden 2	23	22.9	0.50%	6.8	6.3	6.85%	–1.06	–0.94	11.30%

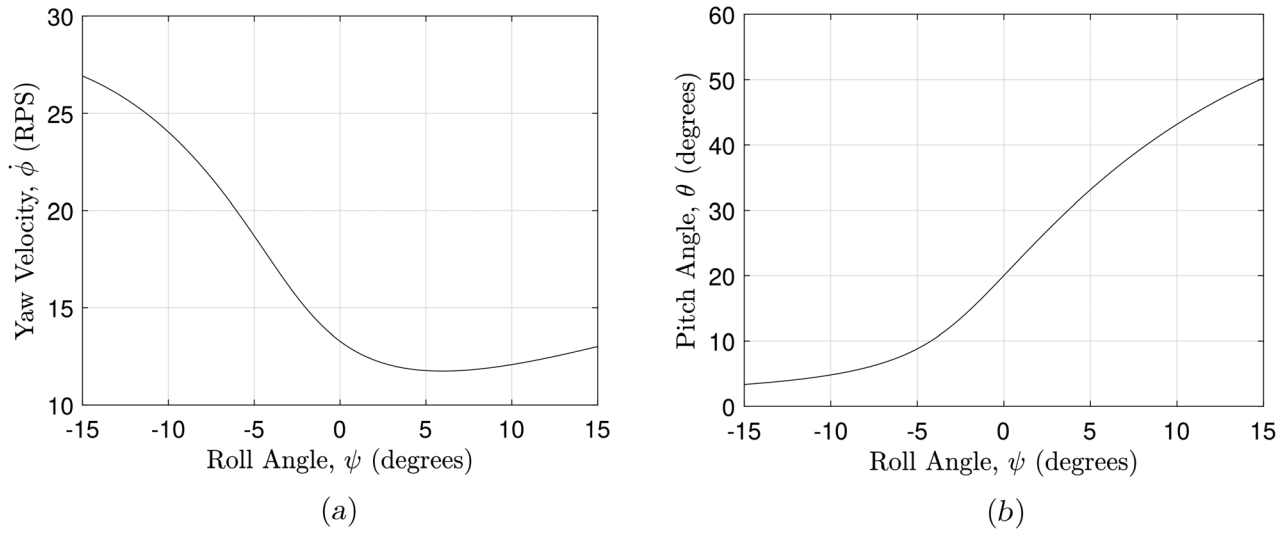

Fig. 5 Steady-state behavior over range of roll angles: (*a*) yaw velocity and (*b*) pitch angle

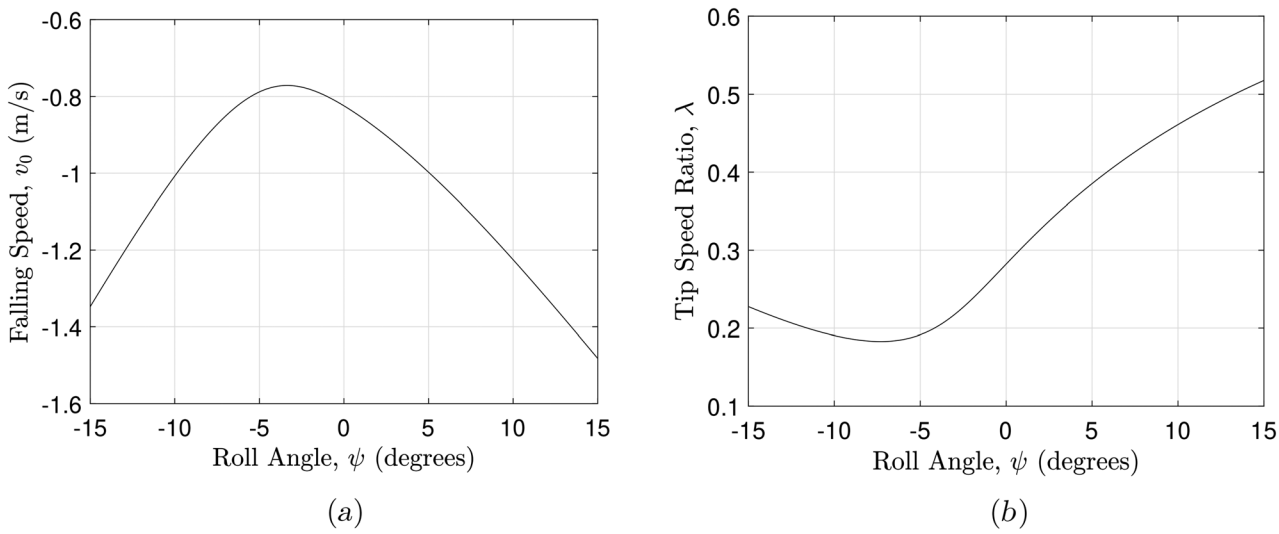

Fig. 6 Steady-state behavior over range of roll angles: (*a*) terminal velocity and (*b*) tip speed ratio

Table 4 Samara modeled results W/variable ψ (deg): θ (deg), $\dot{\phi}$ (rev/s), and v_0 (m/s)

	ψ_{opt}	θ_{mod}	$\dot{\phi}_{\text{mod}}$	$v_{0\text{mod}}$	f_{opt}	$C_{D_0\text{opt}}$
Samara 1	–0.005	21.6	16.5	–0.50	0.209	0.033
Samara 2	0.062	24.6	12.4	–0.61	0.362	0.225
Samara 3	0.389	19.1	13.0	–0.59	0.423	0.217
Samara 4	0.592	29.8	12.2	–0.94	0.336	0.878
Samara 5	–0.006	19.9	15.1	–0.92	0.330	0.794
Norberg	0.172	20.0	13.1	–0.83	0.246	0.126
Holden 1	0.438	24.0	12.1	–0.88	0.262	0.224
Holden 2	–0.396	23.0	6.4	–0.94	0.664	0.704

presented as a constant input. The resulting dynamic model is given in Eqs. (11) and (12). Transient simulation results for θ and $\dot{\theta}$ as well as $\dot{\phi}$ and v_0 are presented in Figs. 7 and 8, respectively. Case 1 (bold) shows the model response with all initial conditions set to 0 (i.e., $\{\theta\ \dot{\theta}\ \dot{\phi}\ v_0\} = \{0\,0\,0\,0\}$). Case 2 (dashed) has initial conditions of $\theta = 45$ deg, $\dot{\theta} = 0.175$ rad/s, $\dot{\phi} = 4$ rev/s, and $v_0 = -0.4$ m/s.

For the dynamic responses of θ, $\dot{\theta}$, $\dot{\phi}$, and v_0, an aggressive stabilization is observed before smoothing out at approximately 0.5 s. The following smooth dynamic settles into steady autorotation within the first second. Special attention should be given to the response of v_0 which at approximately 0.25 s achieves maximum descent speed. Past this point, the samara slows to its autorotative terminal velocity. The steady values of the dynamic simulation show complete agreement with those of the steady-state model, as expected.

The equilibrium of autorotation can be viewed as a balancing of counteracting yawing moments along the span of a rotor-craft blade. This effect is visualized in Fig. 9 which displays the moment provided by each blade element of a samara. For the presented case (case 1), the entire blade provides a moment to increase the rotation of the samara. This effect reduces over time until steady-state is reached. It can be seen that at 1 s an approximately equal region of positive and negative moment is present, suggesting equilibrium. This result agrees with the predicted performance of helicopter blades in autorotation [22].

Observation of samaras found in nature and simulation of the presented model from various initial conditions has suggested the autorotational equilibrium of a single-winged samara is characterized by a large region of attraction. An investigation of samara stability will be presented in Secs. 4 and 5.

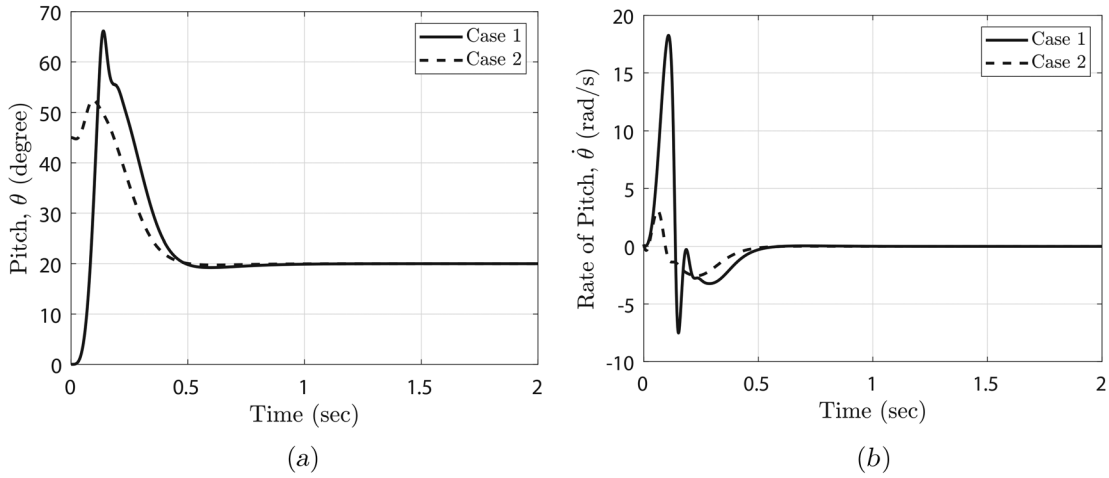

Fig. 7 Samara dynamic response: (*a*) pitch and (*b*) rate of pitch

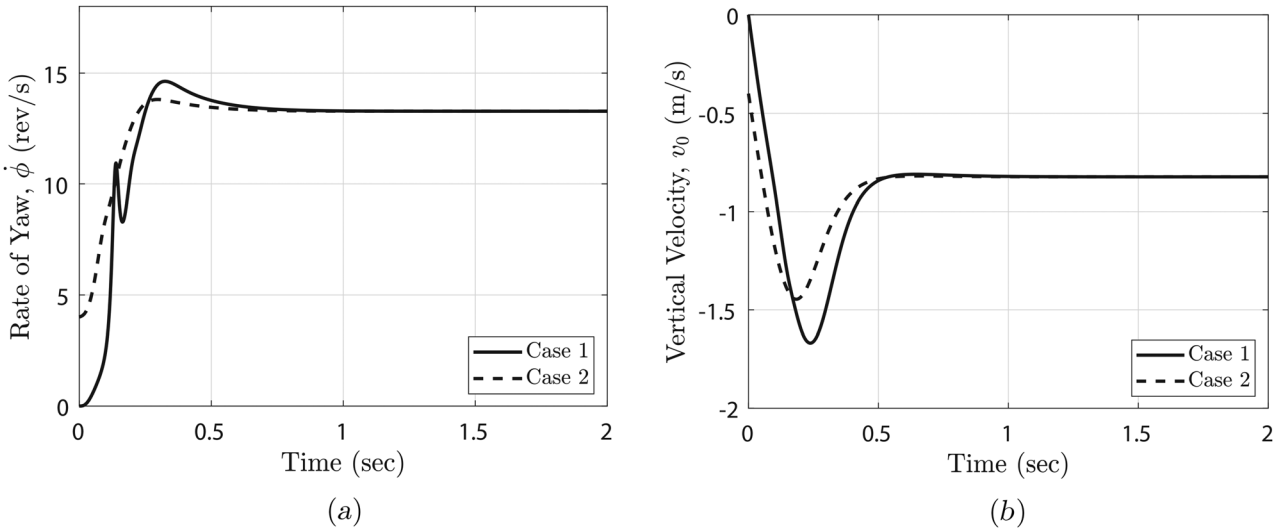

Fig. 8 Samara dynamic response: (*a*) yaw and (*b*) vertical velocity

4 A Necessary Condition for the Existence of Autorotational Equilibrium

In this section, a necessary condition for the existence of an autorotational equilibrium of the falling samara is derived based on the equations of motion presented in this paper. Under steady autorotation, $\dot{\phi}$, θ, and v_0 are constant. Note that the solution of steady autorotation can only exist if there exists a solution λ for Eq. (20), as r varies over the span $r \in [r_0, r_f]$. Substituting the expressions of M_{y_3} and M_{z_3} from Eq. (16) and (17), respectively, Eq. (20) can be rewritten as

$$M_{z_3}\cos\psi + M_{y_3}\sin\psi = 0$$
$$\Rightarrow \frac{1}{2}\rho\int_{r_0}^{r_f} w(r)r||\mathbf{U}_\infty||^2[\sin(\alpha-\psi)C_L - \cos(\alpha-\psi)C_D]dr = 0 \tag{21}$$

In Eq. (21), $||\mathbf{U}_\infty||^2 > 0$ and $w(r) > 0$ for $r \in [r_0, r_f]$. Therefore, for Eq. (21) to be valid, it is necessary that there exists an $r \in (r_0, r_f)$ where

$$\sin(\alpha-\psi)C_L - \cos(\alpha-\psi)C_D = 0 \tag{22}$$

is satisfied. From Eq. (15), it can be shown that

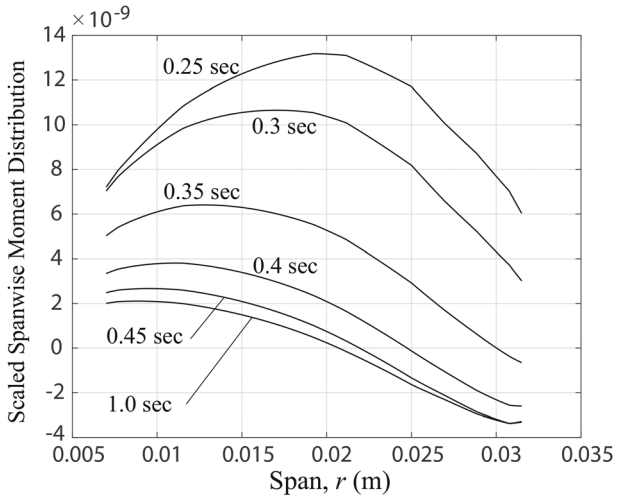

Fig. 9 Scaled yawing moment along span of blade (case 1)

$$\sin(\alpha-\psi)=-\frac{v_0\cos\theta}{||\mathbf{U}_\infty||}=-\frac{v_0}{\sqrt{r^2\dot{\phi}^2+v_0^2}},$$
$$\cos(\alpha-\psi)=\frac{r\dot{\phi}}{\sqrt{r^2\dot{\phi}^2+v_0^2}} \tag{23}$$

From Eqs. (19) and (23), Eq. (22) reduces to

$$\sin\alpha+\frac{C_{D_0}}{2\pi\sin\alpha}=-\frac{v_0}{r\dot{\phi}} \quad\Rightarrow\quad \sin^2\alpha-\frac{\lambda}{\chi}\sin\alpha+\gamma=0,$$
$$\gamma=\frac{C_{D_0}}{2\pi} \tag{24}$$

where λ and χ are defined in Eq. (14). Equation (24) is quadratic in $\sin\alpha$, and for an autorotational equilibrium to exist it is necessary that the solution of $\sin\alpha$ is real. Thus, the following:

$$\frac{\lambda}{\chi}>2\sqrt{\gamma} \tag{25}$$

is a necessary condition. From Eqs. (14) and (24), and since the solution of Eq. (25) must be in the range $r\in(r_0,\,r_f)$, substituting $\chi=r/R$ yields the following requirements:

$$r_0<r<\frac{\lambda R}{2\sqrt{\gamma}} \quad\Rightarrow\quad r_0<\frac{\lambda R}{2\sqrt{\gamma}} \quad\Rightarrow\quad \gamma<\frac{\lambda^2R^2}{4r_0^2} \quad\Rightarrow$$
$$C_{D_0}<\frac{\pi\lambda^2R^2}{2r_0^2} \tag{26}$$

The above condition on C_{D_0} is useful since it places a requirement on the drag coefficient. Since typically at steady-state $\lambda\approx0.25$, as observed in the presented study, and since $r_0=0.2R$ is considered, Eq. (26) suggests, $C_{D_0}<2.45$. For a steady-state $\lambda\approx0.28$, as obtained in Fig. 6(*b*) for $\psi=0\,\text{deg}$, the requirement becomes $C_{D_0}<3.08$. The necessary condition can thus be reduced to an upper bound on C_{D_0}. The bound is conservative as evident from typical model values shown in Tables 1 and 4. The necessary condition for autorotation leads to another interesting deduction if $\psi=0\,\text{deg}$ is imposed. This case is of importance since the presented model has shown good predictive capabilities under this condition. From Eqs. (14) and (23)

$$\psi=0\,\text{deg}\;\Rightarrow\;\sin\alpha=-\frac{v_0}{\sqrt{r^2\dot{\phi}^2+v_0^2}}=\frac{\lambda/\chi}{\sqrt{1+(\lambda/\chi)^2}}$$

Substituting the above expression of $\sin\alpha$ into the necessary condition in Eq. (24)

$$\left(\frac{\lambda}{\chi}\right)^2+\gamma\left[1+\left(\frac{\lambda}{\chi}\right)^2\right]=\left(\frac{\lambda}{\chi}\right)^2\sqrt{1+\left(\frac{\lambda}{\chi}\right)^2} \tag{27}$$

From the above transformed necessary condition, which is valid for the case when $\psi=0\,\text{deg}$, a solution for (λ/χ) can exist in Eq. (27) only if $\gamma>0$, implying $C_{D_0}>0$. The term C_{D_0} in the drag coefficient of Eq. (19) is thus a critical component in determining autorotational equilibrium. Section 5 presents a stability analysis of the autorotational equilibrium.

5 Stability Analysis

The stability analysis presented in this section is based on the coefficients of lift and drag formulations of Eq. (19). For $\psi=\dot{\psi}=0$, the nonlinear dynamics of Eq. (11) can be expressed in state-space form as

$$\frac{d}{dt}\begin{bmatrix}\theta\\ \dot{\theta}\\ \dot{\phi}\\ v_0\end{bmatrix}=\begin{bmatrix}\dot{\theta}\\ -M_{y3}/I_{y3y3}-\dot{\phi}^2\sin\theta\cos\theta\\ M_{z3}/\left(I_{y3y3}\cos\theta\right)+2\dot{\phi}\dot{\theta}\sin\theta/\cos\theta\\ -g+F_{z3}\cos\theta/m\end{bmatrix}=\begin{bmatrix}f_1\\ f_2\\ f_3\\ f_4\end{bmatrix} \tag{28}$$

The linearized dynamics around the equilibrium $(\theta_e,\,\dot{\theta}_e=0,\,\dot{\phi}_e,\,v_{0,e})$ can be expressed as

$$\dot{\tilde{\boldsymbol{X}}}=\mathbf{A_e}\tilde{\boldsymbol{X}},$$
$$\mathbf{A_e}=\left.\begin{bmatrix}0 & 1 & 0 & 0\\ \frac{\partial f_2}{\partial\theta} & \frac{\partial f_2}{\partial\dot{\theta}} & \frac{\partial f_2}{\partial\dot{\phi}} & \frac{\partial f_2}{\partial v_0}\\ \frac{\partial f_3}{\partial\theta} & \frac{\partial f_3}{\partial\dot{\theta}} & \frac{\partial f_3}{\partial\dot{\phi}} & \frac{\partial f_3}{\partial v_0}\\ \frac{\partial f_4}{\partial\theta} & \frac{\partial f_4}{\partial\dot{\theta}} & \frac{\partial f_4}{\partial\dot{\phi}} & \frac{\partial f_4}{\partial v_0}\end{bmatrix}\right|_e=\begin{bmatrix}0 & 1 & 0 & 0\\ A_{21} & A_{22} & A_{23} & A_{24}\\ A_{31} & A_{32} & A_{33} & A_{34}\\ A_{41} & A_{42} & A_{43} & A_{44}\end{bmatrix} \tag{29}$$

where, $\tilde{\boldsymbol{X}}=\left[(\theta-\theta_e)\;\;\dot{\theta}\;\;\left(\dot{\phi}-\dot{\phi}_e\right)\;\;(v_0-v_{0,e})\right]^T$ and the expressions for $A_{i,j}$, $i=2,3,4$ and $j=1,2,3,4$ are given in the Appendix. The characteristic equation of $\mathbf{A_e}$ is

$$\begin{aligned}&s^4-(A_{22}+A_{33}+A_{44})s^3+(A_{22}A_{33}+A_{33}A_{44}+A_{44}A_{22}-A_{23}A_{32}\\&\quad-A_{34}A_{43}-A_{42}A_{24}-A_{21})s^2\\&\quad+(-A_{22}A_{33}A_{44}-A_{23}A_{34}A_{42}-A_{43}A_{32}A_{24}+A_{22}A_{34}A_{43}\\&\quad+A_{33}A_{24}A_{42}+A_{44}A_{23}A_{32}\\&\quad+A_{21}A_{33}-A_{23}A_{31}+A_{21}A_{44}-A_{24}A_{41})s\\&\quad+(A_{21}A_{34}A_{43}-A_{21}A_{33}A_{44}+A_{23}A_{31}A_{44}-A_{23}A_{34}A_{41}\\&\quad+A_{24}A_{41}A_{33}-A_{24}A_{31}A_{43})=0\end{aligned} \tag{30}$$

An analytical study of the eigenvalues of $\mathbf{A_e}$ (e.g., using Routh stability [23]) is tedious considering the complexity of the individual expressions of $A_{i,j}$, as evident from Eqs. (A1)–(A12). To simplify the analysis the following decoupled matrices are considered as substitutes for the stability analysis. The two candidate matrices are

$$\mathbf{A_e^*}=\begin{bmatrix}0 & 1 & 0 & 0\\ A_{21} & A_{22} & 0 & 0\\ 0 & 0 & A_{33} & A_{34}\\ 0 & 0 & A_{43} & A_{44}\end{bmatrix},\quad \bar{\mathbf{A}}_\mathbf{e}=\begin{bmatrix}0 & 1 & 0 & 0\\ A_{21} & A_{22} & 0 & A_{24}\\ 0 & 0 & A_{33} & 0\\ A_{41} & A_{42} & 0 & A_{44}\end{bmatrix} \tag{31}$$

In $\mathbf{A_e^*}$, the dynamics of θ and $\dot{\theta}$ are decoupled from that of $\dot{\phi}$ and v_0, thus resulting in two (2×2) linear systems. In $\bar{\mathbf{A}}_\mathbf{e}$, the dynamics of θ, $\dot{\theta}$ and v_0 are decoupled from that of $\dot{\phi}$, resulting in one (3×3) and a scalar dynamical system. In both cases, the stability analysis is simplified. To evaluate which simplification is better suited for analysis, a numerical root-locus study is performed. The four main parameters of the samara model, namely, the mass m, the blade radius R, the mass distribution factor f, and the drag factor C_{D_0} are varied by $\pm30\%$ and the corresponding eigenvalues are plotted for the original linearized system $\mathbf{A_e}$ and the simplified ones, $\mathbf{A_e^*}$ and $\bar{\mathbf{A}}_\mathbf{e}$. The eigenvalue variations and comparisons are shown in Fig. 10. It is noted that for all parameter perturbations in Fig. 10, the eigenvalues of $\mathbf{A_e}$, which is the original linearized system, are well-approximated by those of $\mathbf{A_e^*}$. Furthermore, they are better approximated by the eigenvalues of $\mathbf{A_e^*}$ than those of $\bar{\mathbf{A}}_\mathbf{e}$. The same observation is made for decoupling the dynamics of the descent velocity, v_0, from that of θ, $\dot{\theta}$, and $\dot{\phi}$. The decoupling in the

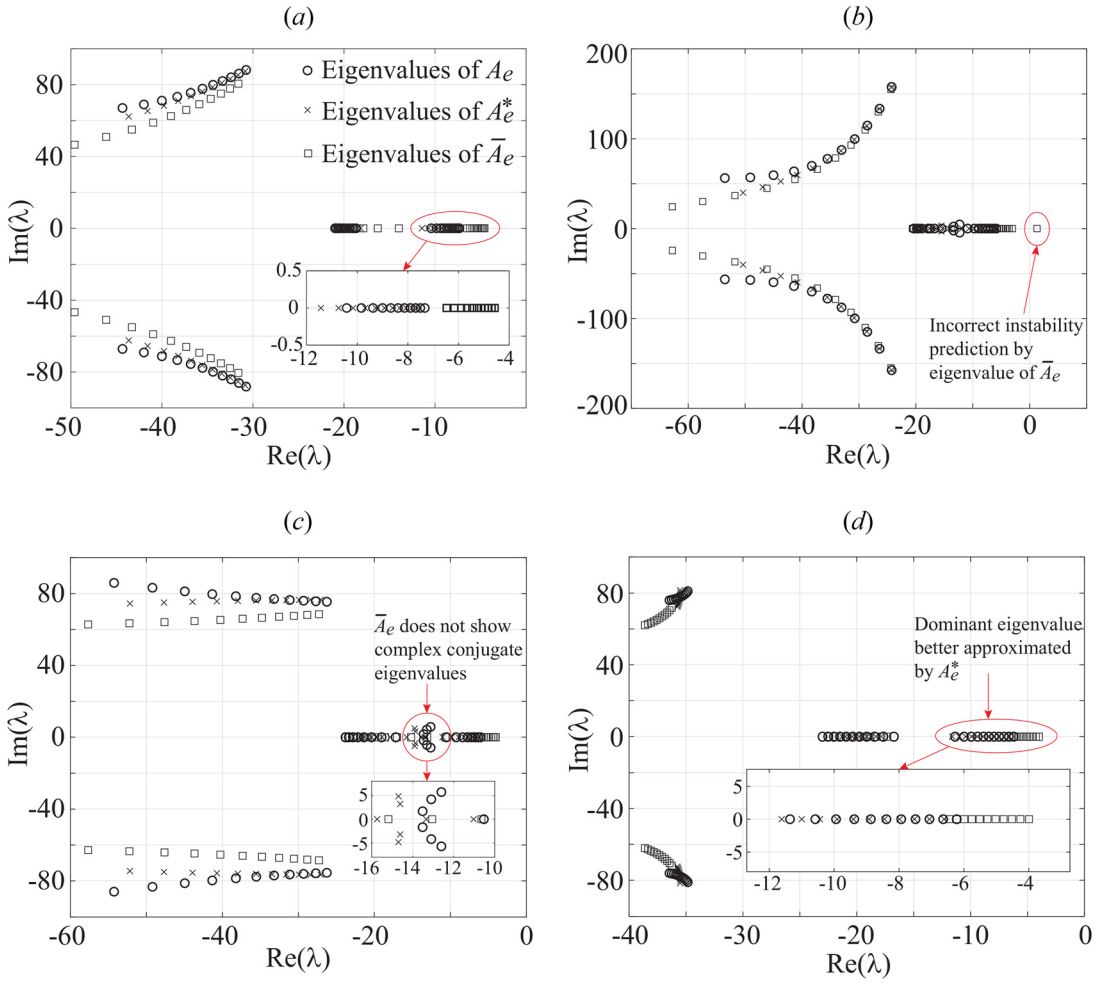

Fig. 10 Eigenvalue variation in $\mathbf{A_e}$, $\mathbf{A_e^*}$ and $\bar{\mathbf{A}}_\mathbf{e}$ due to $\pm 30\%$ parameter perturbations in (*a*) *m*, (*b*) *R*, (*c*) *f*, and (*d*) C_{D_0}

form of two (2×2) linear systems, as in $\mathbf{A_e^*}$, thus provides a way to do a tractable stability analysis of the original linearized system while better retaining the characteristics of $\mathbf{A_e}$ than $\bar{\mathbf{A}}_\mathbf{e}$. It is also evident from Fig. 10 that the off-block-diagonal entries of $\mathbf{A_e}$, with respect to the block-diagonal form of $\mathbf{A_e^*}$, do not produce enough effect on its eigenvalues to induce instability.

Based on the observations above, the conditions that ensure stability of the autorotational equilibrium of the samara using $\mathbf{A_e^*}$ can be analyzed. First, consider the stability of the subsystem

$$\mathbf{A}^*_{\mathbf{e,1}} = \begin{bmatrix} 0 & 1 \\ A_{21} & A_{22} \end{bmatrix} \tag{32}$$

The stability of $\mathbf{A}^*_{\mathbf{e,1}}$ is ensured by the following necessary and sufficient conditions:

$$A_{21} < 0 \quad \text{and} \quad A_{22} < 0 \tag{33}$$

Consider the expression of A_{21} given in Eq. (A1). All terms of Eq. (A1) will be negative if $v_{0,e} < 0$, $\dot{\phi}_e > 0$, $0 < \theta_e < \pi/4$, $C_{D_0} > 0$, $I_{y3y3} > 0$ and if all integral terms in Eq. (A1) are positive. Note that the samara geometry, aerodynamic properties, and equilibrium conditions ensure that the above requirements are satisfied and thereby $A_{21} < 0$ provided $0 < \theta_e < \pi/4$. Next consider the expression of A_{22} given in Eq. (A2). It can be expressed as

$$\begin{aligned} A_{22} = &-\frac{\pi\rho\dot{\phi}_e \cos\theta_e}{I_{y_3y_3}} \int_{r_0}^{r_f} r^3 w(r) dr \\ &- \frac{C_{D_0}\rho \cos\theta_e}{2I_{y_3y_3}} \int_{r_0}^{r_f} r^2 w(r) \sqrt{r^2\dot{\phi}_e^2 + v_{0,e}^2}\, dr \\ &- \frac{C_{D_0}\rho\, v_{0,e}^2 \cos\theta_e}{2I_{y_3y_3}} \int_{r_0}^{r_f} \frac{r^2 w(r)}{\sqrt{r^2\dot{\phi}_e^2 + v_{0,e}^2}} dr \\ &- \frac{\pi\rho\, v_{0,e}^2 \cos\theta_e}{I_{y_3y_3}} \int_{r_0}^{r_f} \left(3 - \frac{v_{0,e}^2}{r^2\dot{\phi}_e^2 + v_{0,e}^2}\right) \frac{r^2 w(r)}{\sqrt{r^2\dot{\phi}_e^2 + v_{0,e}^2}} dr < 0 \end{aligned} \tag{34}$$

This concludes that $A_{22} < 0$ since all terms in Eq. (34) are negative, including the last term which is negative because $v_{0,e}^2/(r^2\dot{\phi}_e^2 + v_{0,e}^2) \leq 1$. Thus, the negativity of A_{22} is also guaranteed by the samara geometry, aerodynamic properties, and equilibrium conditions. This establishes the stability of the subsystem $\mathbf{A}^*_{\mathbf{e,1}}$. Next, consider the subsystem $\mathbf{A}^*_{\mathbf{e,2}}$, given by

$$\mathbf{A}^*_{\mathbf{e,2}} = \begin{bmatrix} A_{33} & A_{34} \\ A_{43} & A_{44} \end{bmatrix} \tag{35}$$

It can be verified that $\mathbf{A}^*_{\mathbf{e,2}}$ is stable if and only if

$$A_{33} + A_{44} < 0 \quad \text{and} \quad A_{33}A_{44} > A_{34}A_{43} \tag{36}$$

Consider the first condition in Eq. (36). From Eq. (A7), A_{33} can be expressed as

$$A_{33} = -\frac{\pi\rho\, v_{0,e}^2 \cos\theta_e}{I_{y_3y_3}} \int_{r_0}^{r_f} \left(\frac{v_{0,e}^2}{r^2\dot{\phi}_e^2 + v_{0,e}^2} \right) \frac{r^2 w(r)}{\sqrt{r^2\dot{\phi}_e^2 + v_{0,e}^2}} dr \tag{37}$$

$$\begin{aligned} &- \frac{C_{D_0}\rho\cos\theta_e}{2I_{y_3y_3}} \int_{r_0}^{r_f} r^2 w(r) \sqrt{r^2\dot{\phi}_e^2 + v_{0,e}^2}\, dr \\ &- \frac{C_{D_0}\rho\dot{\phi}_e^2\cos\theta_e}{2I_{y_3y_3}} \int_{r_0}^{r_f} \frac{r^4 w(r)}{\sqrt{r^2\dot{\phi}_e^2 + v_{0,e}^2}} dr < 0 \end{aligned} \tag{38}$$

In Eq. (38), $A_{33} < 0$ since each term is negative around the equilibrium. Similarly, from Eq. (A12), A_{44} can be expressed as

$$\begin{aligned} A_{44} = &- \frac{\pi\rho\dot{\phi}_e\cos^3\theta_e}{m} \int_{r_0}^{r_f} r w(r) dr \\ &- \frac{C_{D_0}\rho\, v_{0,e}^2\cos^3\theta_e}{2m} \int_{r_0}^{r_f} \frac{w(r)}{\sqrt{r^2\dot{\phi}_e^2 + v_{0,e}^2}} dr \\ &- \frac{C_{D_0}\rho\cos^3\theta_e}{2m} \int_{r_0}^{r_f} w(r) \sqrt{r^2\dot{\phi}_e^2 + v_{0,e}^2}\, dr \\ &- \frac{\pi\rho\, v_{0,e}^2\cos^3\theta_e}{m} \int_{r_0}^{r_f} \left(3 - \frac{v_{0,e}^2}{r^2\dot{\phi}_e^2 + v_{0,e}^2} \right) \frac{w(r)}{\sqrt{r^2\dot{\phi}_e^2 + v_{0,e}^2}} dr < 0 \end{aligned} \tag{39}$$

In Eq. (39), $A_{44} < 0$ since each term is negative around the equilibrium, including the last term since $v_{0,e}^2/(r^2\dot{\phi}_e^2 + v_{0,e}^2) \le 1$. Thus, the condition $A_{33} + A_{44} < 0$ in Eq. (36) is satisfied in the neighborhood of the autorotational equilibrium. Next, consider the second term of Eq. (36). Here, first note from Eqs. (38) and (39) that $A_{33}A_{44} > 0$. Next from Eq. (A11), A_{43} can be expressed as

$$\begin{aligned} A_{43} = &- \frac{\pi\rho\, v_{0,e}\cos^3\theta_e}{m} \int_{r_0}^{r_f} \left(1 - \frac{v_{0,e}^2}{r^2\dot{\phi}_e^2 + v_{0,e}^2} \cdot \frac{r\dot{\phi}_e}{\sqrt{r^2\dot{\phi}_e^2 + v_{0,e}^2}} \right) r w(r) dr \\ &- \frac{C_{D_0}\rho\, v_{0,e}\dot{\phi}_e\cos^3\theta_e}{2m} \int_{r_0}^{r_f} \frac{r^2 w(r)}{\sqrt{r^2\dot{\phi}_e^2 + v_{0,e}^2}} dr > 0 \end{aligned} \tag{40}$$

In Eq. (40), $A_{43} > 0$ since both terms are positive, considering $v_{0,e} < 0$. Next from Eq. (A8), A_{34} can be expressed as

$$\begin{aligned} A_{34} = &\frac{2\pi\rho\, v_{0,e}\cos\theta_e}{I_{y_3y_3}} \\ &\int_{r_0}^{r_f} \left(1 - \frac{r\dot{\phi}_e\left(1 + C_{D_0}/4\pi\right)}{\sqrt{r^2\dot{\phi}_e^2 + v_{0,e}^2}} + \frac{v_{0,e}^2\, r\dot{\phi}_e}{2\left(r^2\dot{\phi}_e^2 + v_{0,e}^2\right)^{1.5}} \right) r w(r) dr \end{aligned} \tag{41}$$

If $A_{34} < 0$, then $A_{34}A_{43} < 0$ and hence the second condition of Eq. (36) would be satisfied. Note from Eq. (41) that since $v_{0,e} < 0$, a conservative condition for $A_{34} < 0$ is

$$\begin{aligned} &\left(1 - \frac{r\dot{\phi}_e\left(1 + C_{D_0}/4\pi\right)}{\sqrt{r^2\dot{\phi}_e^2 + v_{0,e}^2}} + \frac{v_{0,e}^2\, r\dot{\phi}_e}{2\left(r^2\dot{\phi}_e^2 + v_{0,e}^2\right)^{1.5}} \right) \ge 0 \\ \Rightarrow\ & C_{D_0} \le 4\pi \left(\sqrt{1 + \left(\frac{v_{0,e}}{r\dot{\phi}_e}\right)^2} + \frac{\left(\frac{v_{0,e}}{r\dot{\phi}_e}\right)^2}{2\left(1 + \left(\frac{v_{0,e}}{r\dot{\phi}_e}\right)^2\right)} - 1 \right) \end{aligned} \tag{42}$$

Noting that

$$\frac{v_{0,e}}{r_f\dot{\phi}_e} = \frac{v_{0,e}}{0.9R\dot{\phi}_e} \le \frac{v_{0,e}}{r\dot{\phi}_e} \le \frac{v_{0,e}}{r_0\dot{\phi}_e} = \frac{v_{0,e}}{0.2R\dot{\phi}_e} \Rightarrow \frac{\lambda_e}{0.9} \le \frac{v_{0,e}}{r\dot{\phi}_e} \le \frac{\lambda_e}{0.2} \tag{43}$$

Equations (42) and (43) yield the following condition for $A_{34} < 0$, which is more conservative than Eq. (42):

$$C_{D_0} \le 4\pi \left(\sqrt{1 + \left(\frac{\lambda_e}{0.9}\right)^2} + \frac{\left(\frac{\lambda_e}{0.9}\right)^2}{2\left(1 + \left(\frac{\lambda_e}{0.9}\right)^2\right)} - 1 \right) \tag{44}$$

The condition in Eq. (44) is not restrictive. This can be verified by noting that since a typical value of $\lambda_e \approx 0.25$. Substituting this value into Eq. (44) yields $C_{D_0} \le 0.93$. For a steady-state $\lambda \approx 0.28$, as obtained in Fig. 6(*b*) for $\psi = 0$ deg, the requirement becomes $C_{D_0} \le 1.14$. Thus, stability is also dependent on the parameter C_{D_0} in our model and the stability condition on C_{D_0} is more stringent in comparison to the necessary condition of autorotation, as derived in Sec. 4. From the zoomed-in views of Figs. 10(*a*) and 10(*d*), it is evident that the dominant eigenvalue of $\mathbf{A_e}$ is around –9. This would imply a rise-time [23], of about $1.8/9 = 0.2$ s. This matches well with the approximate rise-times in the transient simulations of Figs. 8(*a*) and 8(*b*).

It should be noted that, while there are alternate methods to study the stability of the aforementioned system, such as using the *Gerschgorin circle theorem* [24] or its block analog [25], or even the *small gain theorem* for interconnected systems [26], these analysis yield significantly more conservative stability criteria for this study. It is also arguable that the partial derivatives in Eq. (29) could be numerically determined instead of the analytical approach adopted in this paper. Indeed, the numerical approach was attempted and it was observed these calculations were lacking in convergence. A similar convergence-related observation was made in Ref. [15], which ultimately relied on numerical values based on additional investigations on the accuracy of the numerical process.

6 Conclusions

A simplified and compact model for the steady-state behavior of a single-winged samara has been presented. It has been shown that an assumption of negligible roll angle, $\psi = 0$, is reasonable, and can simulate accurate steady-state and realistic transient behavior. With small, nonzero ψ values, improvements can be made to simulation agreement with data, but these deviations appear to be more correlated with individual morphological differences between samaras as opposed to a general trend of ψ deviation. Experimental results have been shown for five Red Maple samaras to tune and validate the model. The use of two tunable parameters has adequately encapsulated the effects of complex geometry and higher-order aerodynamic phenomena on drag and moment of inertia. Necessary conditions for the existence of an autorotation equilibrium have been analytically derived with further analysis on stability, suggesting ranges of parameters that can be employed in the development of biomimicking aerodynamic mechanisms. The stability analysis reveals that in the neighborhood of the autorotational equilibrium, the eigenvalues of the higher-order coupled system can be well-approximated by two decoupled lower-order systems. This lends itself to a tractable stability analysis which shows the reliance of stability on key parameters of the samara. Furthermore, the compact form of the presented model lends itself well to implementation in aerodynamic control of single-winged crafts. A topic of future interest is the exploration of lateral stability and the effects of wind gusts as well as employing the presented model in a control system.

Funding Data

- National Science Foundation CMMI, USA (Grant No. 1762986; Funder ID: 10.13039/100000001).

Data Availability Statement

The datasets generated and supporting the findings of this article are obtainable from the corresponding author upon reasonable request.

Nomenclature

C_D = coefficient of drag
C_{D_0} = additional drag effects
C_L = coefficient of lift
f = adjustment for mass distribution
F = net force
g = acceleration due to gravity
I = moment of inertia
m = mass
M = net moment
r = radial position
R = blade radius
v_0 = vertical velocity of samara
w = blade width
α = local angle of attack
θ = pitch angle
λ = tip speed ratio
ρ = air density
ϕ = yaw angle
χ = span ratio
ψ = roll angle
ω = angular velocity

Appendix

$$A_{21} = \left.\frac{\partial f_2}{\partial \theta}\right|_e = \frac{\pi\rho\, v_{0,e}\,\dot{\phi}_e \sin 2\theta_e}{I_{y_3y_3}} \int_{r_0}^{r_f} r^2 w(r)dr + \frac{\pi\rho\, v_{0,e}^3 \sin 2\theta_e}{I_{y_3y_3}} \int_{r_0}^{r_f} \frac{rw(r)}{\sqrt{r^2\dot{\phi}_e^2 + v_{0,e}^2}}dr + \frac{C_{D_0}\rho\, v_{0,e}\,\dot{\phi}_e \sin 2\theta_e}{2I_{y_3y_3}} \int_{r_0}^{r_f} rw(r)\sqrt{r^2\dot{\phi}_e^2 + v_{0,e}^2}dr - \dot{\phi}_e^2 \cos 2\theta_e \tag{A1}$$

$$A_{22} = \left.\frac{\partial f_2}{\partial \dot{\theta}}\right|_e = -\frac{\pi\rho\dot{\phi}_e \cos\theta_e}{I_{y_3y_3}} \int_{r_0}^{r_f} r^3 w(r)dr + \frac{\pi\rho\, v_{0,e}^4 \cos\theta_e}{I_{y_3y_3}} \int_{r_0}^{r_f} \frac{r^2 w(r)}{\left(r^2\dot{\phi}_e^2 + v_{0,e}^2\right)^{1.5}}dr - \frac{C_{D_0}\rho\cos\theta_e}{2I_{y_3y_3}} \int_{r_0}^{r_f} r^2 w(r)\sqrt{r^2\dot{\phi}_e^2 + v_{0,e}^2}dr - \frac{\rho\, v_{0,e}^2 \cos\theta_e(6\pi + C_{D_0})}{2I_{y_3y_3}} \int_{r_0}^{r_f} \frac{r^2 w(r)}{\sqrt{r^2\dot{\phi}_e^2 + v_{0,e}^2}}dr \tag{A2}$$

$$A_{23} = \left.\frac{\partial f_2}{\partial \dot{\phi}}\right|_e = -\frac{\pi\rho\, v_{0,e} \cos^2\theta_e}{I_{y_3y_3}} \int_{r_0}^{r_f} r^2 w(r)dr + \frac{\pi\rho v_{0,e}^3\dot{\phi}_e \cos^2\theta_e}{I_{y_3y_3}} \int_{r_0}^{r_f} \frac{r^3 w(r)}{\left(r^2\dot{\phi}_e^2 + v_{0,e}^2\right)^{1.5}}dr - \frac{C_{D_0}\rho\, v_{0,e}\,\dot{\phi}_e \cos^2\theta_e}{2I_{y_3y_3}} \int_{r_0}^{r_f} r^3 w(r)\sqrt{r^2\dot{\phi}_e^2 + v_{0,e}^2}dr - \dot{\phi}_e \sin 2\theta_e \tag{A3}$$

$$A_{24} = \left.\frac{\partial f_2}{\partial v_0}\right|_e = -\frac{\pi\rho\dot{\phi}_e \cos^2\theta_e}{I_{y_3y_3}} \int_{r_0}^{r_f} r^2 w(r)dr + \frac{\pi\rho\, v_{0,e}^4 \cos^2\theta_e}{I_{y_3y_3}} \int_{r_0}^{r_f} \frac{rw(r)}{\left(r^2\dot{\phi}_e^2 + v_{0,e}^2\right)^{1.5}}dr - \frac{C_{D_0}\rho\cos^2\theta_e}{2I_{y_3y_3}} \int_{r_0}^{r_f} rw(r)\sqrt{r^2\dot{\phi}_e^2 + v_{0,e}^2}dr - \frac{\rho\, v_{0,e}^2 \cos^2\theta_e(6\pi + C_{D_0})}{2I_{y_3y_3}} \int_{r_0}^{r_f} \frac{rw(r)}{\sqrt{r^2\dot{\phi}_e^2 + v_{0,e}^2}}dr \tag{A4}$$

$$A_{31} = \left.\frac{\partial f_3}{\partial \theta}\right|_e = 0 \tag{A5}$$

$$A_{32} = \left.\frac{\partial f_3}{\partial \dot{\theta}}\right|_e = \frac{2\pi\rho\, v_{0,e}}{I_{y_3y_3}} \int_{r_0}^{r_f} r^2 w(r)dr + \frac{\pi\rho\, v_{0,e}^3\,\dot{\phi}_e}{I_{y_3y_3}} \int_{r_0}^{r_f} \frac{r^3 w(r)}{\left(r^2\dot{\phi}_e^2 + v_{0,e}^2\right)^{1.5}}dr - \frac{\rho\, v_{0,e}\,\dot{\phi}_e(4\pi + C_{D_0})}{2I_{y_3y_3}} \int_{r_0}^{r_f} \frac{r^3 w(r)}{\sqrt{r^2\dot{\phi}_e^2 + v_{0,e}^2}}dr + 2\dot{\phi}_e \tan\theta_e \tag{A6}$$

$$A_{33} = \left.\frac{\partial f_3}{\partial \dot{\phi}}\right|_e = -\frac{\pi\rho\, v_{0,e}^2 \cos\theta_e}{I_{y_3y_3}} \int_{r_0}^{r_f} \frac{r^2 w(r)}{\sqrt{r^2\dot{\phi}_e^2 + v_{0,e}^2}} dr + \frac{\pi\rho\, v_{0,e}^2 \dot{\phi}_e^2 \cos\theta_e}{I_{y_3y_3}} \int_{r_0}^{r_f} \frac{r^4 w(r)}{\left(r^2\dot{\phi}_e^2 + v_{0,e}^2\right)^{1.5}} dr$$
$$- \frac{C_{D_0}\rho\cos\theta_e}{2I_{y_3y_3}} \int_{r_0}^{r_f} r^2 w(r)\sqrt{r^2\dot{\phi}_e^2 + v_{0,e}^2} dr - \frac{C_{D_0}\rho\dot{\phi}_e^2\cos\theta_e}{2I_{y_3y_3}} \int_{r_0}^{r_f} \frac{r^4 w(r)}{\sqrt{r^2\dot{\phi}_e^2 + v_{0,e}^2}} dr \tag{A7}$$

$$A_{34} = \left.\frac{\partial f_3}{\partial v_0}\right|_e = \frac{2\pi\rho\, v_{0,e}\cos\theta_e}{I_{y_3y_3}} \int_{r_0}^{r_f} r w(r) dr + \frac{\pi\rho\, v_{0,e}^3 \dot{\phi}_e \cos\theta_e}{I_{y_3y_3}} \int_{r_0}^{r_f} \frac{r^2 w(r)}{\left(r^2\dot{\phi}_e^2 + v_{0,e}^2\right)^{1.5}} dr$$
$$- \frac{\rho\, v_{0,e}\dot{\phi}_e\cos\theta_e(4\pi + C_{D_0})}{2I_{y_3y_3}} \int_{r_0}^{r_f} \frac{r^2 w(r)}{\sqrt{r^2\dot{\phi}_e^2 + v_{0,e}^2}} dr \tag{A8}$$

$$A_{41} = \left.\frac{\partial f_4}{\partial \theta}\right|_e = \frac{3\pi\rho\, v_{0,e}\dot{\phi}_e \sin\theta_e\cos^2\theta_e}{m} \int_{r_0}^{r_f} r w(r) dr + \frac{3\pi\rho\, v_{0,e}^3 \sin\theta_e\cos^2\theta_e}{m} \int_{r_0}^{r_f} \frac{w(r)}{\sqrt{r^2\dot{\phi}_e^2 + v_{0,e}^2}} dr$$
$$+ \frac{3C_{D_0}\rho\, v_{0,e}\sin\theta_e\cos^2\theta_e}{2m} \int_{r_0}^{r_f} w(r)\sqrt{r^2\dot{\phi}_e^2 + v_{0,e}^2} dr \tag{A9}$$

$$A_{42} = \left.\frac{\partial f_4}{\partial \dot{\theta}}\right|_e = -\frac{\pi\rho\dot{\phi}_e\cos^2\theta_e}{m} \int_{r_0}^{r_f} r^2 w(r) dr + \frac{\pi\rho\, v_{0,e}^4\cos^2\theta_e}{m} \int_{r_0}^{r_f} \frac{r w(r)}{\left(r^2\dot{\phi}_e^2 + v_{0,e}^2\right)^{1.5}} dr$$
$$- \frac{\rho\, v_{0,e}^2\cos^2\theta_e(6\pi + C_{D_0})}{2m} \int_{r_0}^{r_f} \frac{r w(r)}{\sqrt{r^2\dot{\phi}_e^2 + v_{0,e}^2}} dr$$
$$- \frac{C_{D_0}\rho\cos^2\theta_e}{2m} \int_{r_0}^{r_f} r w(r)\sqrt{r^2\dot{\phi}_e^2 + v_{0,e}^2} dr \tag{A10}$$

$$A_{43} = \left.\frac{\partial f_4}{\partial \dot{\phi}}\right|_e = -\frac{\pi\rho\, v_{0,e}\cos^3\theta_e}{m} \int_{r_0}^{r_f} r w(r) dr + \frac{\pi\rho\, v_{0,e}^3\dot{\phi}_e\cos^3\theta_e}{m} \int_{r_0}^{r_f} \frac{r^2 w(r)}{\left(r^2\dot{\phi}_e^2 + v_{0,e}^2\right)^{1.5}} dr$$
$$- \frac{C_{D_0}\rho\, v_{0,e}\dot{\phi}_e\cos^3\theta_e}{2m} \int_{r_0}^{r_f} \frac{r^2 w(r)}{\sqrt{r^2\dot{\phi}_e^2 + v_{0,e}^2}} dr \tag{A11}$$

$$A_{44} = \left.\frac{\partial f_4}{\partial v_0}\right|_e = -\frac{\pi\rho\dot{\phi}_e\cos^3\theta_e}{m} \int_{r_0}^{r_f} r w(r) dr - \frac{\rho\, v_{0,e}^2\cos^3\theta_e(6\pi + C_{D_0})}{2m} \int_{r_0}^{r_f} \frac{w(r)}{\sqrt{r^2\dot{\phi}_e^2 + v_{0,e}^2}} dr$$
$$- \frac{C_{D_0}\rho\cos^3\theta_e}{2m} \int_{r_0}^{r_f} w(r)\sqrt{r^2\dot{\phi}_e^2 + v_{0,e}^2} dr + \frac{\pi\rho\, v_{0,e}^4\cos^3\theta_e}{m} \int_{r_0}^{r_f} \frac{w(r)}{\left(r^2\dot{\phi}_e^2 + v_{0,e}^2\right)^{1.5}} dr \tag{A12}$$

References

[1] Burrows, F., 1975, "Wind-Borne Seed and Fruit Movement," New Phytol., **75**(2), pp. 405–418.
[2] Augspurger, C., 1986, "Morphology and Dispersal Potential of Wind-Dispersed Diaspores of Neotropical Trees," Am. J. Botany, **73**(3), pp. 353–363.
[3] Augspurger, C., and Franson, S., 1987, "Wind Dispersal of Artificial Fruits Varying in Mass, Area, and Morphology," Ecology, **68**(1), pp. 27–42.
[4] Green, D., 1980, "The Terminal Velocity and Dispersal of Spinning Samaras," Am. J. Botany, **67**(8), pp. 1218–1224.
[5] Green, D., and Johnson, E., 1990, "The Aerodynamics of Plumed Seeds," Funct. Ecol., **4**(1), pp. 117–125.
[6] Green, D., and Johnson, E., 1993, "Seed Mass and Dispersal Capacity in Wind-Dispersed Diaspores," OIKOS, **67**(1), pp. 69–74.
[7] McCutchen, C. W., 1977, "The Spinning Rotation of Ash and Tulip Tree Samaras," Science, **197**(4304), pp. 691–692.
[8] Norberg, R., 1973, "Autorotation, Self-Stability, and Structure of Single-Winged Fruits and Seeds (Samaras) With Comparative Remarks on Animal Flight," Biol. Rev., **48**(4), pp. 561–596.
[9] Ulrich, E., Humbert, J., and Pines, D., 2010, "Pitch and Heave Control of Robotic Samara Micro Air Vehicles," J. Aircr., **47**(4), pp. 1290–1299.
[10] Ulrich, E., and Pines, D., 2012, "Effects of Planform Geometry on Mechanical Samara Autorotation Efficiency and Rotational Dynamics," J. Am. Helicopter Soc., **57**(1), pp. 1–10.
[11] Lentink, D., Dickson, W., van Leeuwen, L., and Dickson, M., 2009, "Leading-Edge Vortices Elevate Lift of Autorotating Plant Seeds," Science, **324**(5933), pp. 1438–1440.
[12] Holden, J., 2016, "Experimental Testing and Computational Fluid Dynamics Simulation of Maple Seeds and Performance Analysis as a Wind Turbine," Master's thesis, University of Cincinnati, Cincinnati, OH.
[13] Limacher, E., 2015, "Samara-Seed Aerodynamics," Master's thesis, University of Calgary, Calgary, AB.
[14] Rosen, A., and Seter, D., 1991, "Vertical Autorotation of a Single-Winged Samara," ASME J. Appl. Mech., **58**(4), pp. 1064–1071.
[15] Seter, D., and Rosen, A., 1992, "Stability of the Vertical Autorotation of a Single-Winged Samara," ASME J. Appl. Mech., **59**(4), pp. 1000–1008.
[16] Yasuda, K., and Azuma, A., 1997, "The Autorotation Boundary in the Flight of Samaras," J. Theor. Biol., **185**(3), pp. 313–320.
[17] Nathan, R., Safriel, U., Noy-Meir, I., and Schiller, G., 1996, "Samara's Aerodynamic Properties in Pinus Halepensis Mill., a Colonizing Tree Species, Remain Constant Despite Considerable Variation in Morphology," Preservation Our World Wake Change, **VIA/B**, Y. Steinberger (Ed.), ISEEQS Pub., Jerusalem, Israel, pp. 553–556.
[18] McConnell, J., and Das, T., 2022, "Reduced Order Modeling of an Autorotating Samara for Steady-State and Dynamic Analysis," IFAC-PapersOnLine, **55**(37), pp. 68–73.
[19] Crimi, P., 1988, "Analysis of Samara-Wing Decelerator Steady-State Characteristics," J. Aircr., **25**(1), pp. 41–47.

[20] Crimi, P., 1996, "Finite Element Analysis of Samara-Wing Decelerator," J. Aircr., **33**(4), pp. 793–802.
[21] White, F. M., 2011, *Fluid Mechanics*, 7th ed., McGraw-Hill, New York.
[22] Leishman, J. G., 2006, *Principles of Helicopter Aerodynamics*, 2nd ed., Cambridge University Press, New York.
[23] Franklin, G. F., Powell, J. D., and Emami-Naeini, A. F., 2019, *Feedback Control of Dynamic Systems*, 8th ed., Pearson, New York.
[24] Horn, R. A., and Johnson, C. R., 2013, *Matrix Analysis*, 2nd ed., Cambridge University Press, New York.
[25] Feingold, D. G., and Varga, R. S., 1962, "Block Diagonally Dominant Matrices and Generalizations of the Gerschgorin Circle Theorem," Pacific J. Math., **12**(4), pp. 1241–1250.
[26] Khalil, H. K., 2002, *Nonlinear Systems*, 3rd ed., Prentice Hall, Upper Saddle River, NJ.